Automated detection of filaments in the large scale structure of the Universe

Roberto E. González[1]⋆ and Nelson D. Padilla[1]

[1]*Departamento de Astronomía y Astrofísica, Pontificia Universidad Católica de Chile, Santiago, Chile*

ABSTRACT

We present a new method to identify large scale filaments and apply it to a cosmological simulation. Using positions of haloes above a given mass as node tracers, we look for filaments between them using the positions and masses of all the remaining dark-matter haloes. In order to detect a filament, the first step consists in the construction of a backbone linking two nodes, which is given by a skeleton-like path connecting the highest local dark matter (DM) density traced by non-node haloes. We estimate the characteristic DM density between two skeleton-candidate haloes using two approximations, i) the Voronoi tessellation density when the distance between haloes is similar or smaller than the sum of their virial radii, and ii) when the distance is larger, using a proxy of the minimum DM density between the two haloes assuming NFW profiles. The filament quality is defined by a density and gap parameters characterising its skeleton, and filament members are selected by their binding energy in the plane perpendicular to the filament. This membership condition is associated to characteristic orbital times; however if one assumes a fixed orbital timescale for all the filaments, the resulting distributions of filament thickness and integrated mass are consistent with the results using the full binding energy condition. Therefore, this simplified set of conditions allows the method to be applied to observational data with no dynamical information, while ensuring a reduced amount of systematic biases. We test the method in the simulation using massive haloes($M > 10^{14}h^{-1}M_{\odot}$) as filament nodes, and study several statistical properties of the resulting filaments. The main properties for the highest quality filaments corresponding to a 33% of the total sample are, i) their lengths cover a wide range of values of up to $150h^{-1}$Mpc, but are mostly concentrated below $50h^{-1}$Mpc; ii) their distribution of thickness peaks at $d = 3.0h^{-1}$Mpc and increases slightly with the filament length; iii) their nodes are connected on average to 1.879 ± 0.21 filaments for $\simeq 10^{14.1}M_{\odot}$ nodes; this number increases with the node mass to $\simeq 2.73 \pm 0.026$ filaments for $\simeq 10^{14.9}M_{\odot}$ nodes; iv) on average, the central density along the filaments starts at almost a hundred times the average density in the regions surrounding the nodes and then drops to about a few times the mean density at larger distances, where it remains roughly constant over 20 to 80% of the filament length (this result may depend on the filament length); v) there is a strong relation between length, quality and how straight a filament is, where shorter filaments are those characterised by higher qualities and more straight-line like geometries.

Key words: large scale structure of Universe.

1 INTRODUCTION

The large scale distribution of galaxies and dark matter(DM) shows a web-like structure composed by clusters,

walls, filaments and void regions, and is usually referred to as the cosmic web. These structures can be easily detected by eye in numerical DM simulations or in the observed distribution of galaxies in large surveys such as the Sloan Digital Sky Survey (York et al. 2000, SDSS).

For clusters and voids, there are several well established automated identification methods which have been

---

⋆ E-mail: regonzar@astro.puc.cl (REG); npadilla@astro.puc.cl (NDP)

broadly used, such as the Friend-of-Friends algorithm for halo/cluster detection (Davis et al. 1985, FOF), and the Padilla, Ceccarelli & Lambas (2005) algorithm for reliable detection of voids. In the case of filaments and walls this task is markedly difficult since, in general, there is still no clear consensus on how to characterise them; filaments and walls show complex 3D shapes.

There are different approaches to the study of filaments. From the theoretical point of view it was found that the gravitational collapse of matter on large scales leads to the formation of sheets and filaments (Zel'dovich 1970). Bond et al. (1996) studied tidal fields in the large-scale structure (LSS) and showed how these produce filamentary structures.

There are several sets of filaments which have been identified and characterised by eye in both simulations and observations. Colberg, Krughoff & Connolly (2005) identified by eye 228 filaments between massive neighbouring haloes in a DM simulation, and described several interesting statistical properties using this sample. In observations, Pimbblet et al. (2004) and Porter et al. (2008) identified filaments in large surveys by eye, and dark matter (DM) filaments were also be detected between clusters of galaxies using weak lensing techniques (Mead et al. 2002). In x-ray observations, it has also been possible to detect hot gas filaments connecting clusters (Scharf et al. 2000).

The study of statistics and the topology of the galaxy distribution with the aim to search for filaments starts very early, with studies by Zel'dovich, Einasto & Shandarin (1982), Shandarin & Zel'dovich (1983), and Einasto et al. (1984). Options to automate the search of filaments include the use of statistics on the morphology of structures, such as Minkowski functionals, minimal spanning trees (MST), percolation methods and shapefinders (see review by Martínez & Saar 2002). The minimum spanning tree method was introduced in cosmology by Barrow et al. (1985). This produces a unique graph which connects points of a process without closed loops, but describes mainly the local nearest-neighbour distribution and is unable to provide a full characterisation of the LSS. Shapefinders (Sahni et al. 1998) have also been used to identify filaments.

In three dimensions, the morphology of a compact manifold can be characterised by four Minkowski functionals: volume, surface area, integrated mean curvature and integrated gaussian curvature. It is possible to define a number of quantities related to those functionals; if a set of positions of galaxies or haloes is characterised by particular values of ratios between the Minkowski functionals, it is very likely that it will show a filamentary shape (Bharadwaj et al. 2000), but this does not guarantee a true detection of a filament or that all the selected members actually belong to the filament.

Another algorithm for the detection of filaments was proposed by Pimbblet (2005) based on the assumption that the orientations of constituent galaxies along such filaments are non-isotropic. This method works well on straight filaments with separations smaller than 15Mpc/h, as has been shown in their application to the 2-degree Field Galaxy Redshift Survey (2dFGRS, Colless et al. 2001).

The Skeleton method (Eriksen et al. 2004; Novikov et al. 2006) has proven useful for the detection of possible filamentary structures in continuous two dimensional density fields. The skeleton is determined by segments parallel to the gradient of the field connecting saddle points to local maxima. The method involves interpolation and smoothing of the point distribution, introducing the kernel band-width as an extra parameter in the procedure of estimating the density field. Extending this work to three dimensions, Sousbie et al. (2008) found good agreement between detected skeletons and eye detections in a numerical DM simulation. By using the Hessian matrix eigenvalues they were able to detect filamentary structures (See also Aragón-Calvo et al. 2007a, 2007b). Bond, Strauss & Cen (2009) also use the Hessian matrix of the galaxy density field smoothed on different scales to characterise the morphology of the LSS in mock catalogues and in the SDSS (Stoughton et al. 2002); they use their detected structures to determine the typical scales where filaments, clumps and walls are dominant.

The Candy Model used by Stoica et al. (2005), is a two-dimensional marked point process where segments serve as marks. This method has been adapted to three dimensions and also improved to a more general Bisous Model (Stoica et al. 2008), producing detections in very good agreement with the result of eye detection in tracing filamentary structures using only galaxy positions (as in the method we will present). However, the detection and thickness of the resulting filaments is only given by a coverage threshold (percent of total points, to be included in filaments).

The spin and orientation of haloes in filaments has been studied by Aragón-Calvo et al. (2007b) and Zhang et al. (2009). They use a Multi-scale Morphology Filter (MMF) and compute the Hessian Matrix eigenvalues in a density field smoothed on different scales, to divide the full volume of their samples into cluster, filament and wall like structures. However, this method, as well as other Hessian matrix based methods, is affected by a lack of an ability to determine the thickness of filaments, and are difficult to apply to observational data, where one needs to define whether a galaxy is a member of a cluster, filament or void.

In this work we propose a new automated method to detect filaments which builds upon ideas of several of the methods mentioned previously. A novel feature of the method is that it is designed to search for filaments using nodes (corresponding to haloes or galaxy clusters as in Colberg, Krughoff & Connolly 2005) selected by applying lower limits on their mass (or proxy for mass). This new method aims to be applicable to discrete halo or galaxy positions even when these are so sparsely distributed that it is not possible to define a smooth density field, or that the Hessian matrix cannot be computed with an adequately high accuracy. This makes it particularly suitable for observational data such as the 2dFGRS or SDSS. In addition, we replace the smoothing scales and filament coverage thresholds by parameters with improved physical meaning. In this new approach a filament quality depends on parameters related to the relative density and gaps of the filament skeleton, and its members are identified as the haloes or galaxies with binding energies with respect to the filament in the plane perpendicular to its skeleton. In order to apply this method to observational data we will use numerical simulations to calibrate the binding condition using objects with

a collapse time and radius that can be computed even when dynamical information is not available.

This paper is organised as follows. Section 2 presents the numerical simulation on which we perform our automated search for filaments. The method is presented in Section 3, which also includes details on the measurement of the local density field, and describes the input parameters of the algorithm. Section 4 presents the results and Section 5 concludes this work with our conclusions.

2 THE NUMERICAL SIMULATION

We use a cosmological DM simulation with parameters corresponding to the concordance ΛCDM model (cold dark-matter, $\Omega_b = 0.045$, $\Omega_{DM} = 0.235$, $\Omega_{DE} = 0.72$, $h = 0.72$, $\sigma_8 = 0.847$, & $n = 1$), 500^3 particles and a periodic cube side of 250Mpc/h. At $z = 0$ we find $176,041$ haloes and subhaloes in the mass range $1.4 \times 10^{11} h^{-1} M_\odot < M < 1.5 \times 10^{15} h^{-1} M_\odot$, identified using the AHF code (Knollmann & Knebe 2009). For the detection of filaments, we select as nodes a total of 427 haloes with $M > 10^{14} h^{-1} M_\odot$. The node pairs that will be the candidates for filament search are constructed using neighbour nodes, which are easily obtained using Voronoi Tessellations(VT hereafter, to be explained in more detail in the next section). We obtain a total of $3,075$ node pairs with separations $< 65 h^{-1}$Mpc; Figure 1 shows all the node pairs in a slice of the simulation. In the next section we will apply the filament detection method to each of these node pairs.

3 METHOD

Our filament detection method is described in this section. Even though we will apply it to a numerical simulation, it can be extended to observational datasets with redshift information since it can be set to produce filament samples while only requiring galaxy positions and proxies for their host dark-matter halo masses (virial masses, luminosities in different bands, etc). We will not attempt to find all the filamentary structures in the simulation, only those filament segments generated between haloes above a given mass threshold (node pairs). Therefore, smaller filaments associated to less massive nodes will be missed if they are not in the path (or part) of the selected nodes.

3.1 Density field

We obtain the density and density gradient field using VT, in a similar approach to that adopted by Aragón-Calvo et al. (2007b) where they compute the density field using Delaunay Tessellation Field Estimator (Shaap & van de Weygaert 2000). In the present study we make use of the neighbour information for all the haloes to trace the density field as well as to compute a fast proxy for the density gradient vector field. VT also allows us to obtain the immediate neighbours of each halo (or galaxy if applied to observational data). The Voronoi Tessellation (Voronoi 1908) technique is one of the best adaptive methods to recover a precise density field from a discrete distribution of points, with clear advantage over the method used

in Smoothed Particle Hidrodynamic or other interpolation based techniques (Pelupessy et al. 2003).

We compute the VT for the halo distribution defining a cellular-like structure, where each halo is associated to a region (or voronoi cell) in which any point inside this region is nearest to that halo than to any other. This voronoi cell defines a volume which we use along with the halo mass to define a very precise and adaptive measure of the density of the cell. We also use a first order smoothing of the density field by calculating the mean density of the central and neighbour VT cells.

The estimates of density for the DM haloes in our simulation use their measured virial mass. In many cases, the Voronoi cell containing high mass haloes in dense environments are smaller in volume than the sphere given by its central halo virial radius. This indicates that in these cases we are over-estimating the local density. The opposite occurs in cells of haloes in voids and filament outskirts, where we can under-estimate the local density surrounding these haloes. In the high density end, this problem is not important in our case since we do not include in our method haloes inside the virial radius of tracer nodes. In low density regions where the voronoi cells of haloes are always much larger than their virial spheres, we avoid the problem present in the Voronoi density estimate by using an approximation assuming Navarro, Frenk & White (1997, NFW) profiles.

For a smooth density field, such as is the case of fields traced by DM particles, the Hessian matrix can be computed with high accuracy to find the filament components easily. But the process is more complicated in the case of having only the positions of haloes and their virial masses. This is due to the sparse coverage of haloes, their variable masses, and the loss of information regarding the mass located beyond the virial radii of haloes. In order to understand the importance of these issues we will look at the relation between average halo to neighbour separation (D_{IP}) and its voronoi cell volume.

In order to recover the real density field using only halo positions, one needs to take into account that,

• In high density environments the voronoi cell volume is related to the local mean inter-particle distance, i.e., the mean neighbour distance D_{IP}. The left panel of Figure 2 shows a very tight relation between these two quantities for the full halo population. In the figure, the dashed line shows the $V \propto D_{IP}^3$ relation, which is very useful for halo detection methods such as FOF (Davis et al. 1985), where the particle separation is used to connect particles above a given density threshold. In the case of having only halo positions, we find that this relation breaks down at lower densities (as can be seen in the left panel of Figure 2). The origin of this departure from the distance vs. volume relation is the complex shapes developed by Voronoi cells at such low densities. This implies that the local clumpiness of a set of particles in low density environments is only poorly related to its density; this may pose a challenge to the search for the backbone of filaments. This effect is negligible when obtaining the density field using DM particles since these typically produce a smoother spatial coverage and therefore a much smaller fraction of these will be surrounded by Voronoi cells with complex shapes.

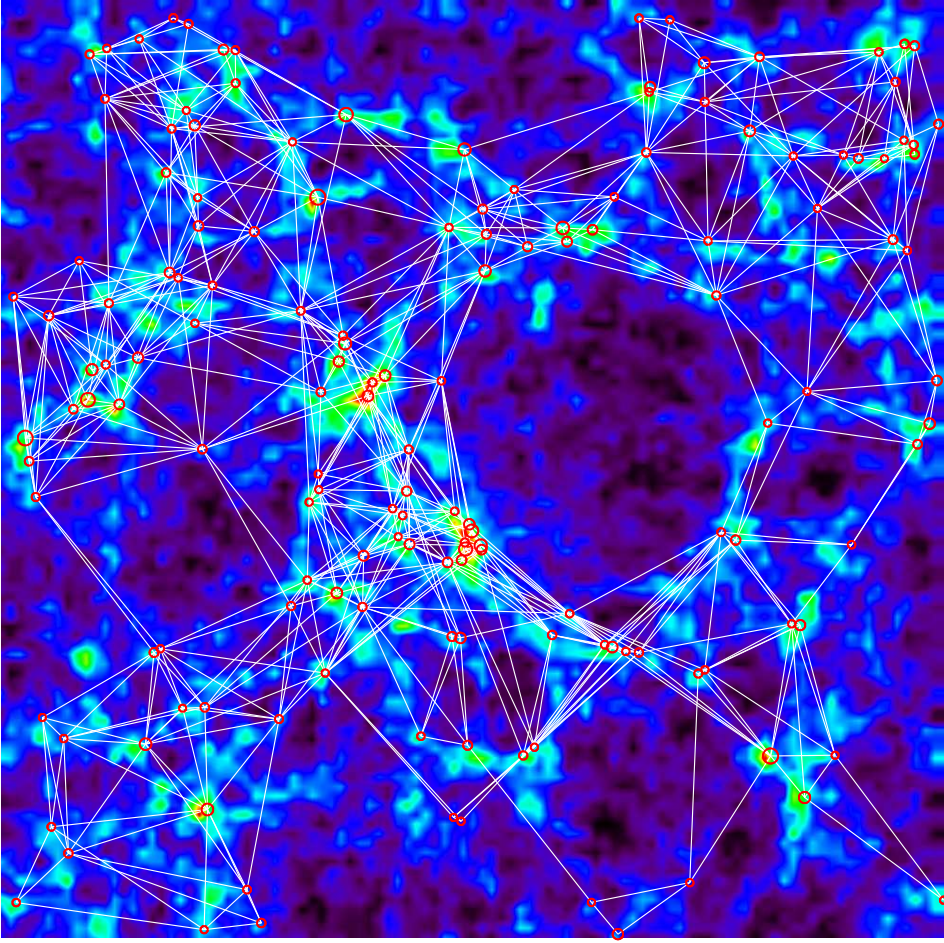• Halo masses introduce additional noise when extending

Figure 1. Density field in the numerical simulation corresponding to a slice $100\text{h}^{-1}\text{Mpc}$ thick. The density is obtained using the halo positions. The red circles enclose the virial radii of the node haloes; white lines connect all the node pairs separated by less than $65\text{h}^{-1}\text{Mpc}$.

the previous relation to $\rho - D_{IP}$ (right panel of Figure 2). In this case, it is possible that the set of haloes with highest VT densities between two nodes do not trace the best possible filament backbone (or the highest DM density path) when compared to a different set of haloes with a smaller inter-halo distance.

Regarding the second item, in order to find the path of highest local DM density connecting two nodes, we need to add constrains on the use of the density field obtained from halo positions. To connect the i-th halo in a filament skeleton to the following neighbour j, such that the characteristic DM density $\rho*$ is a maximum, we will have two cases,

i) $D_{ij} \leqslant R_{VIR}(i) + R_{VIR}(j) : \quad \rho* = k_1\,\rho(j).$

In this case the halo voronoi density is a good proxy for the DM density when the voronoi cell volume is similar to the virial sphere, but may be over-estimated if the cell volume is smaller. This is not a problem for our method since $\rho*$ will naturally increase when haloes are gravitationally linked, and therefore the segment connecting haloes i and j will have the maximum characteristic DM density among the other nearby neighbours.

ii) $D_{ij} > R_{VIR}(i) + R_{VIR}(j) : \quad \rho* = k_2\,\rho(j)\,\eta^{-1}f(M_i, M_j),$

which uses NFW profiles to estimate the minimum DM density between two haloes. In the equation, D_{ij} is the distance between haloes, ρ is the voronoi density, M_i and M_j are the halo masses, the η factor represents the break-down of the relation between inter-halo distance and voronoi cell volume,

$$\eta = \frac{D_{IP}^3}{V_{cell}},$$

$$f(M_i, M_j) \simeq \left(\frac{M_i}{M^*}\right)^{0.13}\left(\frac{1+\Omega}{\Omega}\right)^3, \qquad \Omega = \left(\frac{M_i}{M_j}\right)^{0.376},$$

and k_1 and k_2 are constants intended to provide the continuity between both densities at $\eta = 1$ and $\Omega = 1$; $M^* = 10^{12.5}\text{h}^{-1}M_\odot$ is the constant in the Bullock et al. (2001) concentration vs. mass relation. The η parameter appears naturally in this approximation where its value is usually greater than one; therefore, two haloes with high masses and high voronoi densities will have lower $\rho*$ if their separation is large, as can be the case in regions with a low number density of discrete points.

The DM density between two haloes will be used as segment weights in the search for the path connecting two
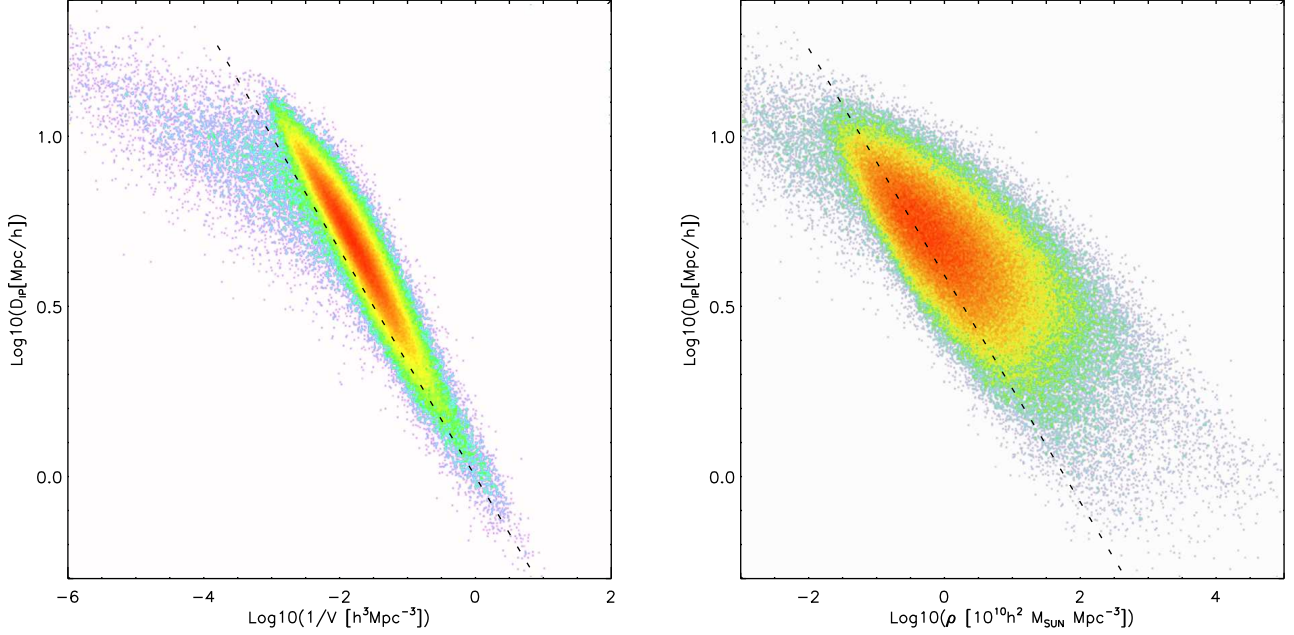
Figure 2. Left panel: Voronoi cell volume vs. mean neighbour separation, D_{IP}, for all the haloes in the simulation. Right panel: Voronoi Density vs. D_{IP} for all the haloes. Dashed lines represent the relation $V = D_{IP}^3$ (left panel); in the right panel it corresponds to $V = median(M_{VIR})/\rho$.

nodes, in a similar way to that used in the search for the shortest path in graph theory; therefore, the filament backbone or skeleton is the result of solving for this graph, which has several different approaches in the literature (Biggs, Lloyd & Wilson, 1986).

3.2 Input parameters

We detect filaments using nodes above a fixed minimum mass. This choice is necessary since the filamentary structure is found at different scales; there are even filaments inside filaments or inside clusters (Bond et al. 1996).

In addition to the minimum node mass, other parameters will be necessary. However, our aim is to involve only the minimum number of parameters possible, which include the following,

• A minimum density threshold for the galaxies or haloes which form the backbone of a filament. When a filament is too thin, or the density contrast above the background is too low, it is possible that the filament is just a group of aligned galaxies which are not bound to any stable structure; these are spurious detections.

• A maximum gap threshold for the galaxies or haloes which define the backbone of the filament. A measure of the gaps in a filament is given by $max(D_{SK}/ < D_{SK} >)$, the maximum distance divided by the average distance between all pairs of consecutive skeleton members of an individual filament. Large values for this parameter imply large gaps between two filament sections. Gaps are an important problem, particularly for low density filaments.

• After the definition of the backbone or skeleton of the filament has been completed, we select the members of the filament. This is done by analysing which neighbours are

gravitationally linked to the filament and will collapse into the skeleton or remain within the filament for at least a given amount of time. We define a timescale t_F, which is the maximum time allowed for the orbit of a halo in the plane perpendicular to the filament, assuming it is gravitationally bound (in this plane). Since the peculiar velocities of the haloes in the numerical simulation are known, we can calculate which haloes are bound to the filament; we use this information to characterise an average timescale and the associated radius out to which bound haloes can be found. This will help to implement this filament identification in the case of observational data with no available information on peculiar velocities.

It is complicated to define physically motivated density and gap thresholds for each filament analogous to the virialisation density for the spherical collapse model. The reasons behind this are the complicated filament shapes and their continuous feeding of their node haloes or clusters. Therefore, we will use these parameters to assess the quality of a filament; filaments will be better defined if their minimum backbone densities are high and their maximum gaps are small.

3.3 Description of the algorithm

We identify filaments in the following way,

(i) We select a node tracer pair.

(ii) We follow the segments of highest local DM density given by the characteristic density $\rho*$. This defines the filament backbone or skeleton. For this we define a set of threshold densities $\rho_{th}(i)$ with $i = 1..N$, in the range set by the minimum and maximum densities in the total density field.
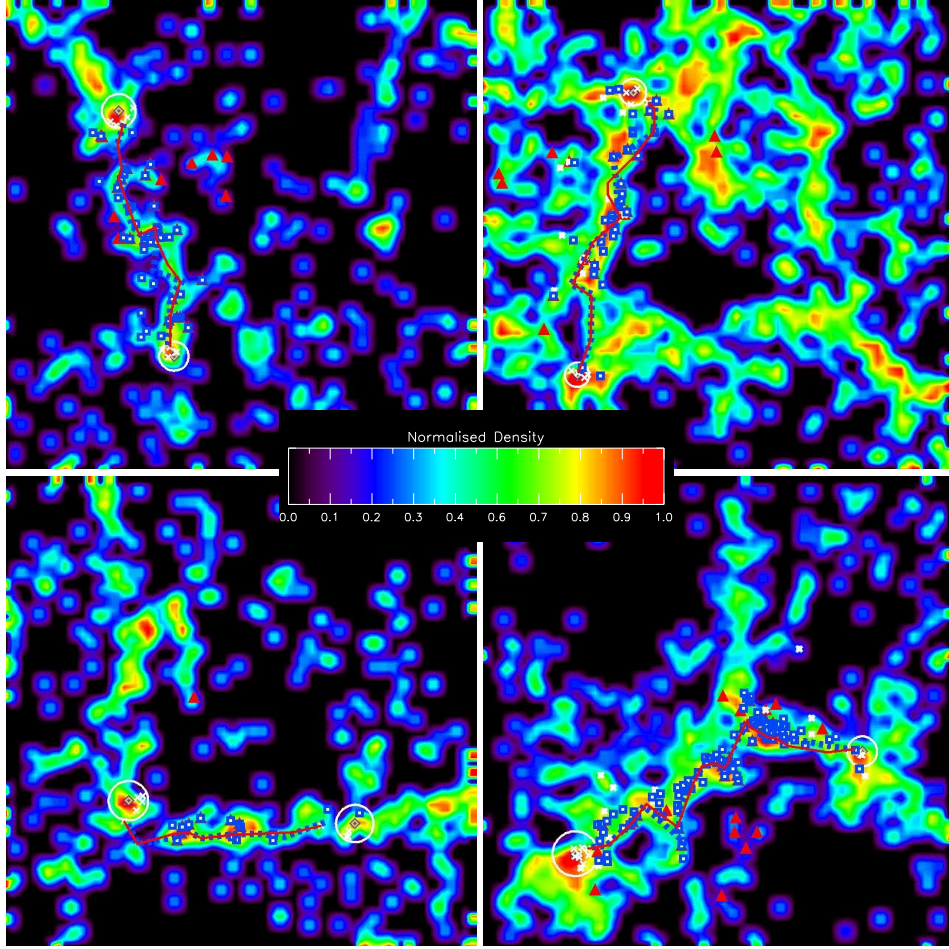
Figure 3. Four examples of detected filaments. The red solid lines show filament skeletons, the blue dashed lines show the re-centred skeleton. The white asterisks correspond to haloes at distances from the filament $r < r_0$, whereas blue squares show haloes at distances $r < r_1$. The red triangles show haloes with $E_P < 0$.

(iii) For each node we generate a list of neighbour haloes just outside the virial radius in the half hemisphere that points to the other node. These neighbours will be labeled as start haloes associated to the node from which we will start the filament search. End haloes will be the neighbours associated with the other node in the node pair in the half hemisphere pointing back to the start node.

(iv) The first attempt is done using the highest density threshold $\rho_{th}(i = 1)$.

(v) The process is iterative selecting the start halo with the highest local DM density with respect to the start node, characterised by a local density greater than $\rho_{th}(i)$. A halo that satisfies this condition becomes part of a possible skeleton, and we search for neighbours of this new skeleton member using the same conditions. If there are no new neighbours satisfying this, we go back to the previous halo from where we will choose a different neighbour to restart the procedure.

(vi) We repeat the last step until any of the end haloes of the other node is reached, or until there are no more haloes satisfying these rules.

(vii) If there is no connection to the other node then we move down to the next density threshold step $\rho_{th}(i + 1)$ characterised by a lower density, and go back to step v.

(viii) We will always find a set of connected points (a filament backbone) between two nodes for a sufficiently low value of ρ_{th} density. Higher values of this density imply stronger filament contrasts.

(ix) We re-centre the local centre of mass of the filament skeleton using its immediate Voronoi neighbours.

Having a well defined backbone, we start adding skeleton neighbours to the filament and computing filament characteristics, in the following way,

(i) For any given halo k we find the nearest skeleton member j.

(ii) We measure the mass contained in a cylinder around the skeleton at the position of the skeleton halo j. The cylinder height is $H = (D_{j,j+1} + D_{j+j-1})/2$ and its radius $R = D_{kj}$. Using this mass and the difference between the average velocities of the haloes within that cylinder, and that of halo k, projected in the plane perpendicular to the cylinder, we compute the total halo energy in the plane, E_P.

(iii) We compute the orbit time t around the cylinder for halo k assuming that the distance D_{kj} is the semi-major axis of the orbit. This timescale only uses information on the potential energy and does not require peculiar velocity data.

(iv) We select all haloes with $E_P < 0$ and calculate their median orbit time t_1; we define r_1 as the radius containing 80% of these haloes. This sample can only be obtained from haloes with peculiar velocity information.

(v) We select all haloes with $E_P < 0$ and $t \leqslant t_F$, with t_F a fixed input parameter, and we define r_0 as the radius where 80% of these haloes are contained. This defines a sample using E_P measurements. Therefore it needs peculiar velocity information to be constructed.

(vi) We select all haloes with $t \leqslant t_F$, and define r_2 as the radius where 80% of these haloes are contained. This selection can be done with position information alone and would therefore be applicable to large observational datasets such as the SDSS.

(vii) Finally, we also select all haloes with $t \leqslant t_1$, and we define r_3 as the radius containing 80% of these haloes. This selection also requires velocity information and is used to assess the importance of the binding energy condition against that of the orbital timescales.

All haloes closer to the skeleton than r_1 will be selected as filament members in the simulation. For observational data r_2 can be used for this purpose.

Figure 4. Filament quality parameters. Minimum skeleton density ($\rho*_{min}$) as a function of the Gap size ($max(D_{SK})/ < D_{SK} >$).

4 RESULTS

Figure 3 shows four detected filaments in the simulation, where the halo density projected onto the $x - y$ plane is shown in a colour scale, the skeleton is shown as red lines, and the re-centred skeleton as blue dashed lines. The nodes are indicated by circles with radii equal to the halo virial radius. White points denote all haloes lying closer than r_0 from the filament skeleton, and blue boxes denote haloes closer than r_1. The red triangles are for haloes with $E_P < 0$. All the filaments contain segments with only either a few or no bound haloes, at least according to our definition.

We bear in mind the possibility of undetected bound haloes since in our energy calculation we do not take into account nearby structures other than the filament. In order to produce a more precise energy calculation one would need to use velocities from other sections of the skeleton instead of only from the nearest skeleton section; filaments show a very complex velocity structure where nodes sometimes move towards each other (they may merge in the future) or away from each other, making filaments suffer stretching, elongations, torsions, and even rotations. However, the incompleteness in the sample of bound haloes should not affect our estimate of the mean effective radius of the filament (r_1) which we use to define filament membership.

In the upper-left and bottom-left panels of Figure 3 the filaments show excellent density contrasts, but also show a gap (near the top node in the upper-left panel, and near the left node in the bottom-left panel). This shows the importance of adopting a gap parameter that allows the existence of these features in selected filaments, to some degree. The filaments in the right panels are of higher quality than those on the left since they do not show important gaps. The section of the filament on the upper-right panel seems not to follow the highest density path due to projection effects (the filament follows a path that enters the page, along the z-axis).
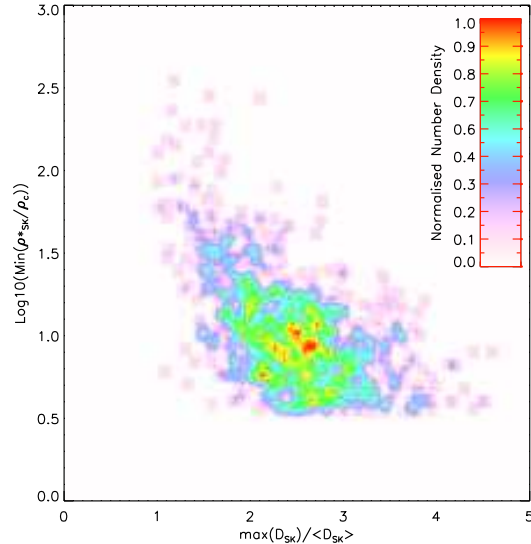
4.1 Filament properties

We apply the method to the numerical simulation described in Section 2, using a minimum skeleton characteristic density $\rho*_{min} = 3\rho_{mean}$ and no gap restriction, limiting the node pairs to relative distances lower than 65Mpc/h.

Out of the 3075 node pairs, 1110 are successfully connected via filaments; we will refer to this first identification as the full sample. We select an additional subsample of 376 filaments which satisfy the additional conditions of $\rho*_{min}$ above the median of the full sample, and $max(D_{SK})/ < D_{SK} >$ below the median; this sample is termed the high-quality subsample and contains 33% of the filaments in the full sample. As was mentioned above, all the detected filaments connect nodes separated by at least the sum of their virial radii. Figure 4 shows the relation between gap and density parameters for the detected filaments which show clear trends of larger gaps at lower densities.

Figure 5 shows the dependence of the quality parameters on node separation for the full sample. There are clear correlations, particularly for filaments shorter than 20Mpc/h, which suggests that shorter node separations produce higher quality filaments.

When studying the properties of the filaments detected using our automated procedure, it will be useful to compare with a previous detection. In particular, we will use the results from Colberg, Krughoff & Connolly (2005) who detected 228 filament in a DM simulation by eye using the smoothed DM density distribution. This filament sample can not be compared directly with our results, since the selection criteria are very different. However, both samples are the result of restricting the search to filaments connecting neighbouring haloes above $10^{14} h^{-1} M_\odot$. The main differences between the two samples arise from, i) Colberg et al. use the distribution of DM particles whereas we use halo positions, ii) they look for filaments using the 12 nearest haloes inside cylinders of $7.5 h^{-1}$Mpc of radius aligned along the node-
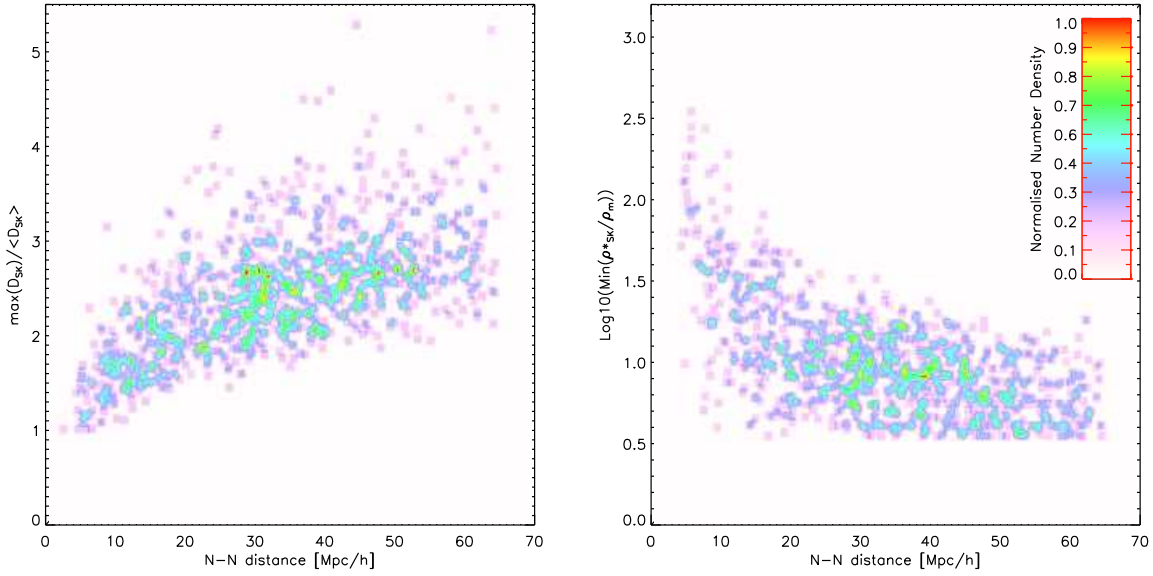
Figure 5. Gap (left) and density (right) quality parameters as a function of node separation.

node axis; in our case we look at all possible neighbour node pairs given by the voronoi tessellation with no volume constrain, iii) Colberg et al. define a true detection based on a visual criterion instead of using quality parameters, iv) they discard node pair connections when other clusters lie inside the innermost $5h^{-1}$Mpc from the node-node axis, and we discard node pair connections when another cluster is closer than 2 times its virial radius to the filament skeleton, v) they divide their sample in straight, off-centre and warped filaments. Therefore, the reader must bear in mind that comparisons between these two samples, are not intended to validate any of the two samples, but to find general filament properties which are less sensitive to different selection criteria.

The node pair connections are given by the voronoi tessellation method, which instead of selecting the n nearest neighbours, chooses neighbours such that the line that connects the pair passes only through the voronoi cell around each node. This ensures than any point along the segment is nearest to one of the two nodes and not to other haloes. The node pair count of the full sample as function of the node separation is shown in Figure 6 as an orange dashed line (the scale of the counts in $5h^{-1}$Mpc bins, is given by the right y-axis). The number of pairs grows almost linearly with the separation almost up to $40h^{-1}$Mpc, and then it decreases for larger node separations. In addition, Figure 6 shows the fraction of node pairs with detected filaments as a function of node separation (left y-axis scale). The full sample (solid black bars) is characterised by a decreasing fraction of connected pairs via filaments as the separation increases; this fraction is nearly 90% for separations shorter than $5h^{-1}$Mpc, and at the largest separations the fraction is reduced to 30%. In the case of the high quality subsample (red bars) the abundance of filaments decreases much faster with fractions below 25% for nodes separated by more than $20h^{-1}$Mpc.

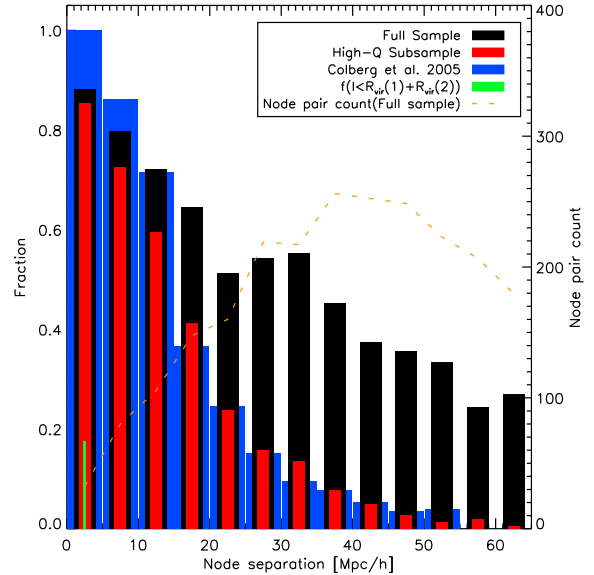Figure 6 also shows the fractional abundance obtained

Figure 6. Fraction of node pairs with detected filaments as function of node pair separation (left y-axis). The green bar on the first bin shows the fraction of node pair connections separated by less than the sum of their virial radii. The total node pair count as a function of node separation for the full sample is shown as an orange dashed line (its scale is indicated on the right y-axis). Black bars show the same fraction for the full sample of quasars, red bars are for the high quality subsample, and the blue bars are for the Colberg et al. sample detected by eye.

by Colberg, Krughoff & Connolly (2005). Even though their selection procedure is different from ours, the resulting dependence of this fraction with pair separation is similar to our results for the high quality subsample. Our method does not consider haloes inside the virial radii of nodes, which means that we do not detect most of the filamentary struc-

ture connecting two nodes separated by distances shorter than the sum of their virial radii. The green bar shown for separations shorter than $5h^{-1}$Mpc in Figure 6 indicates the fraction of node pairs whose separation is shorter than the sum of their virial radii for this range of separations. Most of the pairs represented by the green bar should be connected by filaments (Pimbblet et al. 2004), since these are overlapping bound systems which share matter (i.e. Dietrich et al. 2005; Tittley & Henriksen 2001); furthermore, this behavior should extend up to node separations of a few virial radii (approximately three times the virial radius), which can be associated to the infall region of haloes (Diaferio & Geller 1997; Pivato, Padilla & Lambas 2006). Taking into account the mass resolution of our numerical simulation, the mass in such bridges is mostly in the form of a smooth DM particle distribution, with only a few subhaloes aligned within the bridge. This makes it more difficult to detect them with our method even if we also used subhalo positions; as a consequence we have chosen not to include them in the search. A possible way to overcome this would be to use the DM particle distribution, or to run re-simulations of these regions with higher resolution, enough to resolve several subhaloes per node. The result of such a study would likely change our fraction of detected filaments for node separations below $5h^{-1}$Mpc, which we are underestimating at present; in the case of Colberg, Krughoff & Connolly (2005), they find that most of the halo pairs within this range of separations are connected via filaments.

In the case of filaments detected in the 2dFGRS, Pimbblet et al. (2004) find a fractional abundance of filaments similar to our full sample results; however, their selection criteria are also different from the one we have applied to the simulation. In particular, they also identify filaments by eye and use galaxy positions; therefore in order to make an appropriate comparison it would be necessary to apply our method to realistic 2dFGRS mock catalogues, or directly on the 2dFGRS catalogue.

The main properties of the detected filaments are shown in Figure 7. The top-left panel shows the distributions of t_1 (the median orbit time for haloes with $E_P < 0$), where it can be seen that the high quality filaments are characterised by lower orbit times as expected since these filaments have higher density contrasts and are more concentrated than the full sample. The samples shown in the figure are obtained setting $t_F = 2t_0$ (vertical red dashed line) which is lightly lower than the median of t_1 (indicated by the vertical blue dashed line). This latter value can be used when detecting filaments using observational data since the orbit time distributions shown here are relatively narrow (most of the filaments show similar orbital timescales).

The top-right panel of the figure shows the distributions of the parameters r_0 and r_1 (line types are indicated in the figure key) described in the previous section. As can be seen, a fixed orbit time produces a narrow distribution of r_0 but a wider distribution of r_1 which is obtained using t_1. However, the peaks of both distributions are located at approximately 1.3Mpc/h. It is also noticeable a very slight shift towards smaller radii for the high quality subsample in both cases, an effect which is stronger for the r_1 parameter, indicating a dependence of the t_f value with the quality of the filaments. Therefore, better quality filaments seem to be more concentrated while preserving similar thicknesses

with respect to the filaments in the full sample. In addition, the figure also shows the scale radius r_s computed by Colberg, Krughoff & Connolly (2005) for their sample of filaments (blue bars). In their notation r_s defines the radius where the density profiles of straight filaments starts to follow a r^{-2} relation. Our definition of r_1 indicates a scale radius containing 80% of the bound haloes with orbit times below the median. Even though both definitions are conceptually different, they account for the scale radius where $\approx 50 - 80\%$ of the filament mass is contained. In general, for a given filament, r_s is a more precise computation of the edge of the filament, but requires the DM particle distribution to be calculated; r_1 is easier to compute since it only requires halo positions; however, it can underestimate the filament edges depending on the density profile and density contrast. Therefore, despite the fact that the comparison is made among two quantities with different definitions, as well as different filament samples, it is interesting to note that the distributions of r_1 and r_s show similarities; the latter only shows a slight shift towards larger radii. As can be seen, the characteristic radius which defines a filament shows a narrow distribution with preferred values of 1 to $2h^{-1}$Mpc, even when using filaments of different quality or using a sample of filaments selected by eye. In all cases, however, the lengths of the filaments are similar and are traced by halo nodes with masses above $10^{14}h^{-1}M_\odot$.

The Bottom-left panel of Figure 7 shows the distribution of mass for different filament components (line types are show in the figure key); all the distributions are shown for the full sample of filaments. As can be seen, this tracer node mass selection produces skeletons and filament envelopes less massive than the filament nodes. Both of these two components show similar distributions, with differences only at the low-mass-end. Notice that when using either r_0 or r_1 the resulting filament mass is practically the same. This shows that the detection of filaments using a fixed orbit time (for observational data) will provide reliable filament mass measurements. In the case of the high quality filaments, we find that the masses of the skeleton and the surrounding filament shells are lower than for the complete filament sample, since the former are shorter in length (as can be seen in the bottom-right panel of the figure). We find no clear dependence of filament mass on their node masses.

The bottom-right panel of the figure shows the distributions of node pair separation and of filament extension (line types are indicated in the figure). The filament extension is a measurement of the smoothed filament length, obtained by adding the distances between filament member average positions in a discrete number of segments along the filament. The node separation is on average smaller than the filament length, which indicates that most filaments are warped. The distribution of node pair separation peaks at ≈ 32Mpc/h for the full sample, and at ≈ 15Mpc/h for the high quality subsample. The filament lengths also show a peak at shorter values for the high quality subsample. When analysing the ratio between these two quantities in both, the full and high quality samples, it can be seen that regardless of quality, longer filaments are more warped than shorter filaments; i.e. in the full sample, filaments with node separations below $30h^{-1}$Mpc are on average 13% larger than their node separation; this value increases to 40% for larger node separations. The
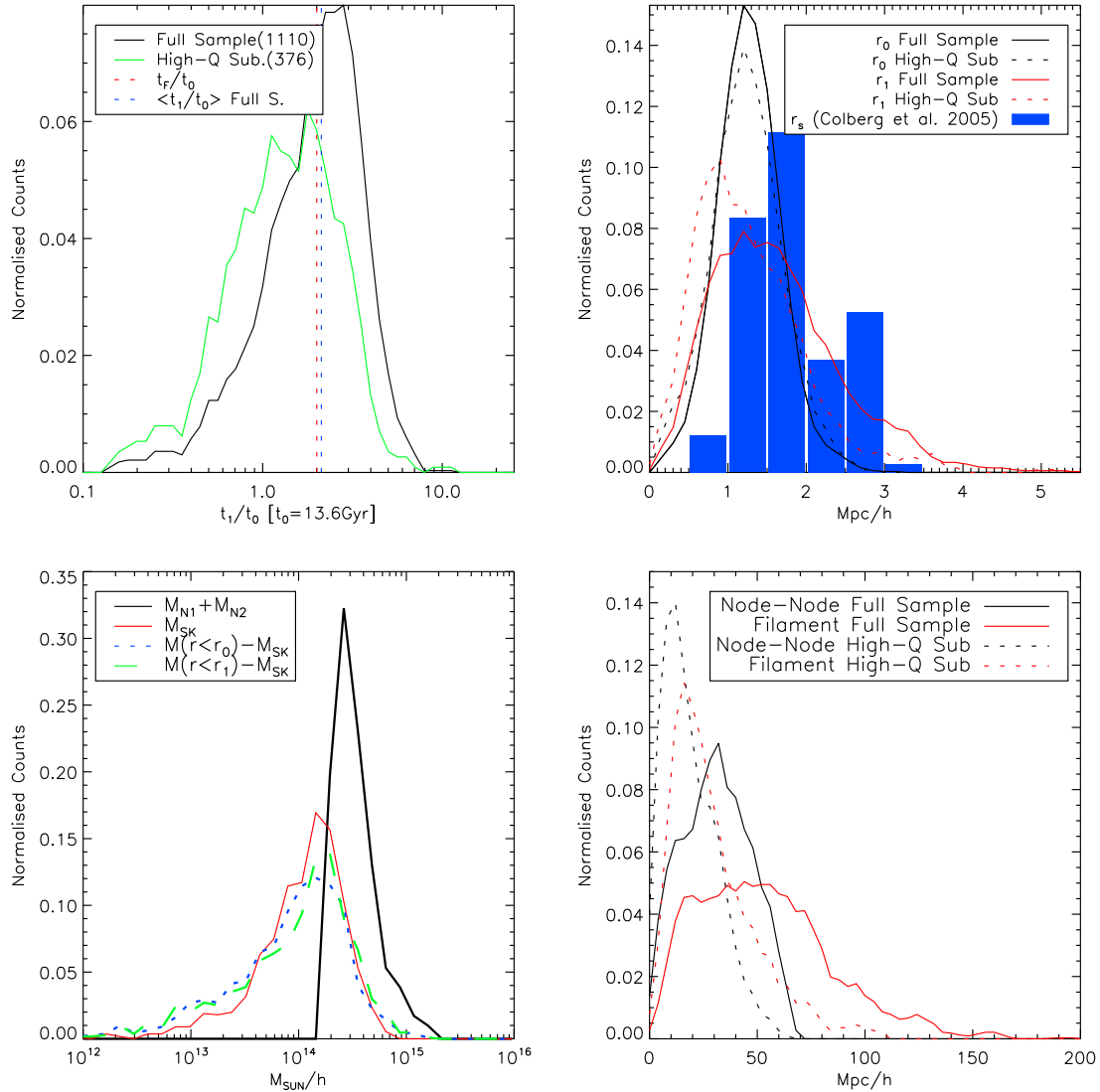
Figure 7. Distribution functions of properties of the detected filaments. The samples of filaments detected using our automated method are shown in different line types (explained in the key). The statistics from the Colberg, Krughoff & Connolly (2005) filament sample are shown as barred histograms.

filaments studied with Shapefinders in the Las Campanas Redshift Survey (Bharadwaj, Bhavsar & Sheth 2004) are characterised by lengths of $50h^{-1}$Mpc to $80h^{-1}$Mpc. In this work, we have found shorter high quality filaments but we have also required node pair separations $< 65h^{-1}$Mpc. It should also be borne in mind that in most cases these filaments are only segments of considerably longer structures with more than two nodes (shapefinders are insensitive to the number of nodes in a filament).

Figure 8 shows the relation between filament thickness (r_1) and filament length. The error bars correspond to the standard deviation in the measurement of the median of r_1, and are computed using the jackknife method. In the high quality subsample, we do not include filaments longer than $80h^{-1}$Mpc due to low filament counts (< 10). As can be seen, there is a trend of thicker filaments for longer filament lengths in both samples (full and high qual-

ity). For the high quality sample, the median values of r_1 for filaments with lengths between 0 and $10h^{-1}$Mpc are $1.11 \pm 0.19h^{-1}$Mpc, and for lengths between 60 and $70h^{-1}$Mpc are $2.01 \pm 0.29h^{-1}$Mpc (a significance of more than 3σ between the longest and shortest filament lengths). This dependence can be a consequence of any or several of the following effects, i) all filaments feed their node haloes and shorter, less massive filaments will exhaust their mass first due to the higher infall velocity and node halo influence over a larger percentage of the filament length (the influence can extend out to several virial radii, Diaferio & Geller 1997), ii) shorter filaments are straighter than longer ones; therefore, in longer, warped filaments concave zones along the skeleton could attract haloes from larger distances, an effect that would be absent in straight-line filaments. The detailed study of this possibility is beyond the scope of this paper and will be treated in a forthcoming paper on fila-
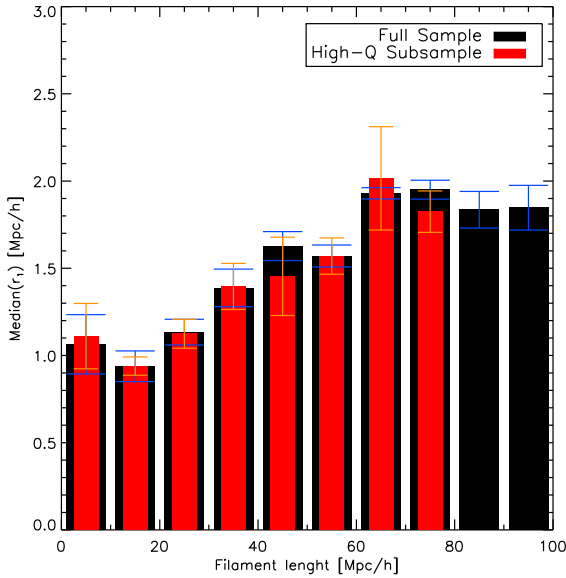
Figure 8. Filament thickness (as measured by r_1) as a function of filament length, for the full sample (black) and high quality subsample (red).

Figure 9. Average longitudinal filament over-density profile obtained using the interpolated voronoi density along the skeleton, as function of the normalised node pair separation. We only show half of the filament length since the profiles are symmetrical, on average.

ment shapes and environments. iii) A higher probability to spuriously assign bound haloes at larger distances from the skeleton for longer filaments, but this is less likely since this effect is also present when using r_0 (which does not depend on a computation of energy) as a thickness indicator.

We study the variation of the mass density along the filament skeletons. Figure 9 shows the average over-density as a function of the normalised node pair separation. It should be borne in mind that as we use the interpolated voronoi density obtained from the halo positions and their viral masses, the density only includes a fraction of the total matter (DM particles beyond the virial radii of haloes are not included in this estimate). We exclude filaments with skeletons containing less than 6 haloes, and the figure only shows half of the filament length since the profiles are symmetrical (on average). The figure shows a similar density profile to those found by Colberg, Krughoff & Connolly (2005), where the over-density rises towards node centres, indicating that on average the infall regions of filaments extent up to 20% of the filament length. At larger distances from the nodes, the overdensity remains at nearly constant values of a few times the average density. The high quality subsample shows a similar profile although with higher density contrasts than the full sample.

We now study the number of filaments connected to individual nodes, and how this depends on the node properties. Figure 10 shows the fraction of filaments connected to $0, 1, 2, ...$ filaments for the full sample (black solid lines), the high quality subsample (red solid lines), and the Colberg, Krughoff & Connolly (2005) results (blue bars). The Poisson error amplitudes are shown as dashed lines for the full and high quality samples. In the full sample, most nodes are connected to $4-6$ filaments, indicating that allowing in all the detected filaments without applying any quality constraints does not provide realistic results, bearing in mind the observational (Pimblett et al., 2005) and numerical
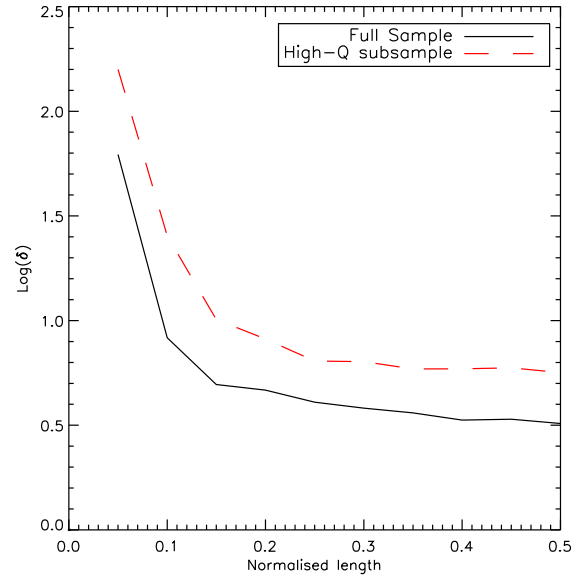
simulation (Colberg et al., 2008) results on this statistics. A better agreement with these estimates is obtained when using the high-quality subsample, in which case most nodes are connected to 2 filaments (and the distribution is very similar to that from the Colberg, Krughoff & Connolly 2005 filaments). In general the number of filaments per node is strongly dependent on the quality of the filaments considered, similar quality thresholds are needed in order to make meaningful comparisons.

Figure 11 shows the average number of filaments per node as a function of the node mass. In all cases this number increases with the node mass. Errors, shown as dashed lines for the full and high quality samples, are obtained using the jackknife method; errors are not shown for the highest mass bin $M > 10^{15} M_\odot$ (cyan hatched region) due to the low number of nodes (10) at this end. Nodes in the high quality subsample are connected to an average of 1.87 ± 0.21 filaments for the lowest mass bin, a number that increases to 2.73 ± 0.26 for $M \simeq 10^{14.9} M_\odot$; the significance of this trend is higher than a 3σ level. This behavior was also observed in the 2dFGRS by Pimbblet et al. (2004), and in a numerical simulation (Colberg, Krughoff & Connolly 2005), clearly indicating that more massive haloes are more likely to have a larger number of connected filaments. This can be associated to the higher amplitude of clustering of more massive haloes characterising random gaussian fluctuation fields in a ΛCDM cosmology Pimbblet et al. (2004).

There is a number of possible issues that could affect this statistics that need to be borne in mind, i) we do not use subhaloes, and therefore node pairs closer than the sum of their virial radii could present filaments which we do not detect. Such close pairs will be more abundant for more massive haloes due to their higher local overdensities, therefore these undetected filaments could populate the high mass end
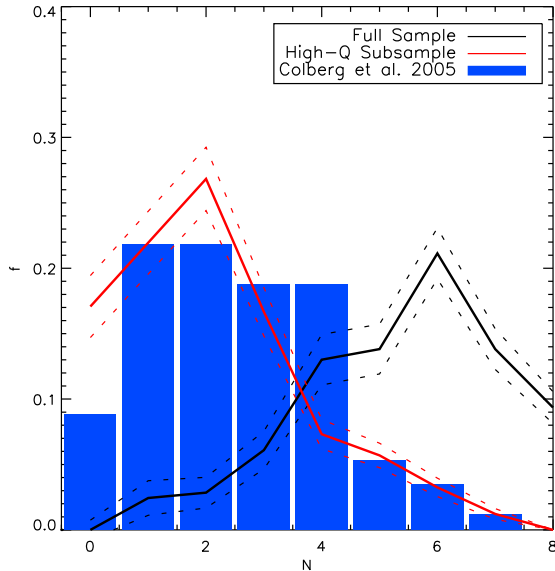
Figure 10. Fraction of nodes connected to N filaments for the full sample of filaments (solid black lines), and for the high quality subsample (solid red lines). In both cases, Poisson errors are shown by the dashed lines. The results from Colberg et al. (2005), are indicated as blue bars.

Figure 11. Number of filament connections per node as function of node mass. Different line types correspond to samples selected in this paper (identified in the figure key); the barred histogram corresponds to the sample of filaments in Colberg, Krughoff & Connolly (2005). The hatched area shows the range of masses containing only 10 node pairs in our numerical simulation.

of the figure 11. ii) To avoid repeated filament segments, we discard filaments which are closer than $2r_{vir}$ to a third node, and Colberg, Krughoff & Connolly (2005) uses a fixed value of $5h^{-1}$Mpc for a similar proximity condition. In both cases we could be missing short filaments in dense environments where nodes are more massive, have larger virial radii and are more strongly clustered; in such places this proximity constrain could be excessive. In order to test this issue, we make a subsample of filaments applying the quality constraints used for the high quality subsample, but allowing filaments closer to a third node when, a) the node pair separation is less than $10h^{-1}$Mpc, b) the minimum density along the filament is greater than 10 times the mean density, c) the sum of the virial radii of the nodes is $> 2.5h^{-1}$Mpc, d) the filaments are close to straight-line shapes. These modifications, in conjunction with the intrinsic properties of voronoi tessellations for the node pair selection, ensures that it is very unlikely that the short filaments in this new sample are repeated segments of other detected filaments. The reason behind this is that for larger node pair separations, there will be larger distances from a node to node axis to a third node. Otherwise the constrain of a common facet between node pair voronoi cells would not be fulfilled. This test subsample is shown as green long dashed line in Figure 11; as can be noticed the relation of filament connections as a function of mass becomes stronger.

4.2   Application to observational data

The density and gap parameters can also be used in filaments detected using galaxy positions. However, it would become more difficult to measure a filament thickness since there seldom is dynamical information to calculate binding energy conditions. The possibil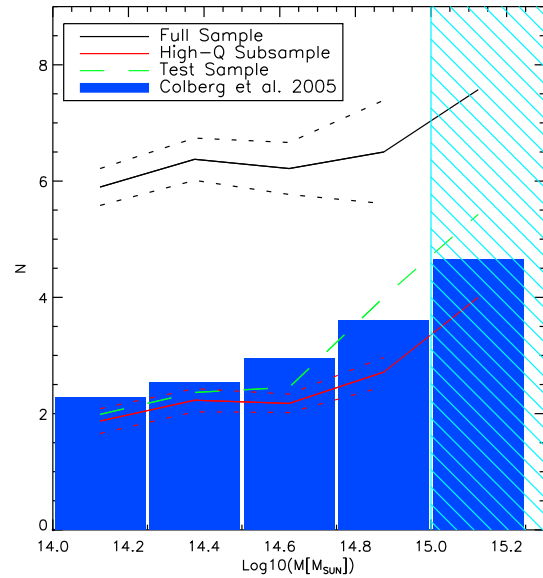ity in these cases is to select filament members assuming that galaxies are bound to the filament and to require orbit times lower than t_F. As can be seen in Figure 7, using a fixed orbit time allows to recover a distribution of r_0 (see Section 3.3 for the definitions of r_0, r_1, r_2 and r_3) which, although slightly narrower, peaks at the same radius as when using the full energy calculation. Also, the recovery of the filament mass is only mildly affected by the use of r_0 or r_1 to select filament members.

Figure 12 shows the relation between r_0 and r_1. As can be seen, there is a linear relation between these quantities for $r_1 < median(r_0)$. Filaments in the high quality subsample show a very similar median r_0 and a slightly lower median r_1 than the full sample, an effect that probably arises from the fact that filaments in the high quality subsample are shorter than in the full sample (see Fig. 7). In the case of the observational data with no dynamical information, the method would only provide measurements of r_2 which, when comparing the vertical long dashed and dotted lines in both panels, can be seen to provide a good approximation to r_0. As the relation between r_0 and r_1 is reliable for thin filaments, $r_2 < 1.2$Mpc/h, thick filaments will probably suffer from an under-estimation of their real thickness, particularly if their quality is low. Regarding r_3 (horizontal dotted lines), it can be seen that their median values are very similar to that of r_1, indicating that if one can estimate the collapse time of bound objects to the filament, the membership obtained using this estimated time provides a good membership criterion.
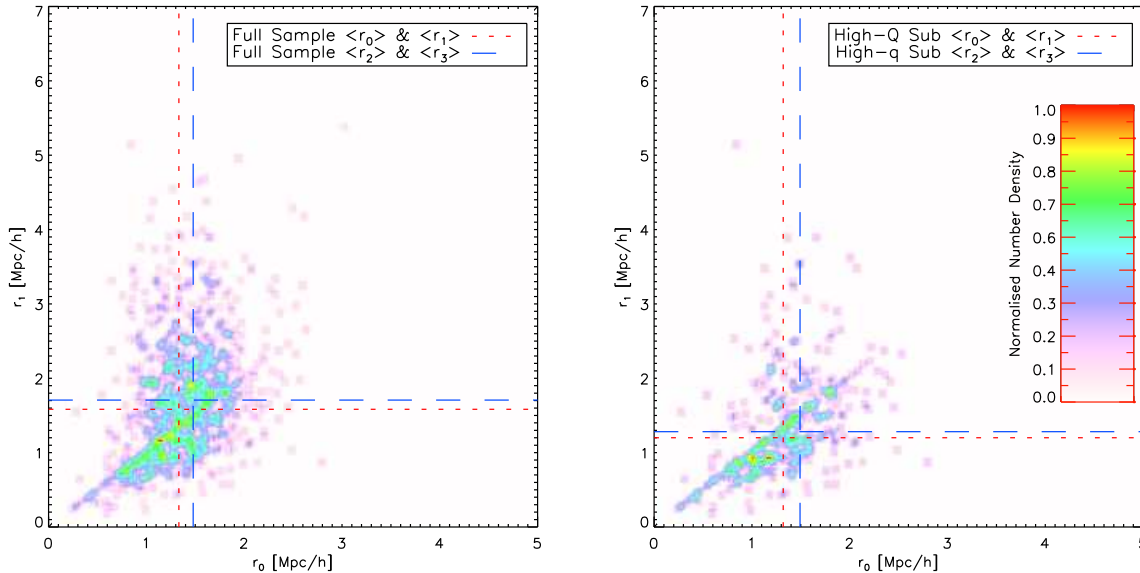
Figure 12. r_0 vs. r_1 for the full sample of filaments (left panel) and for the high quality subsample (right). The vertical and horizontal dotted lines show the median values of r_0 and r_1 (respectively), which are quantities obtained using the full binding energy calculation. The dashed lines show the median values of r_2 and r_3 (vertical and horizontal lines, respectively), which are the equivalent to r_0 and r_1 for the case with no dynamical information (and therefore no energy calculation).

5 CONCLUSIONS

We presented an automated method to detect filaments in cosmological simulations and observational data, using haloes above a fixed mass as tracers of filament nodes. As filaments cannot be treated as virialised structures as in the case of haloes, and as they are characterised by a wide range of lengths, it is a difficult task to identify them automatically. As a result these have been mostly identified by eye. In this work we detect filaments using an automated algorithm that provides two filament quality parameters, i) a minimum skeleton characteristic density, and ii) a gap parameter given by the maximum distance between consecutive skeleton neighbours divided by the average consecutive skeleton neighbour distance in individual filaments. A small gap parameter and a high density parameter, ensure the best quality for a filament. The latter condition is equivalent to request a high density contrast.

In our method we define the width of filaments using the median radius (r_1) that contains the haloes gravitationally bound to the filament in the plane perpendicular to the filament skeleton, and that are characterised by orbit or collapse times below an upper threshold. An application of the method to observational data can be done since the radius r_1 shows a good correlation with r_0 and r_2, obtained assuming that all the galaxies are bound to the filament and computing their orbit times based only on their positions and masses; the members are then selected requiring orbit times below a fixed time t_F. The relation between r_1 and r_2 is one-to-one for thin filaments below $r_0 \approx 1.2$Mpc/h; in thicker filaments r_2 tends to slightly under-estimate the actual width of a filament.

We have presented several filament properties which can be studied in observational catalogues such as the SDSS. In particular, a subsample comprising the 33% highest quality

filaments in our numerical simulations shows very similar properties to filaments detected by eye in numerical simulations by Colberg, Krughoff & Connolly (2005),

• Filament lengths are mostly concentrated below 50h^{-1}Mpc, but can extend to up to 150h^{-1}Mpc

• Shorter filaments are characterised by more straight-line geometries than longer filaments. Filaments with node separations below 30h^{-1}Mpc are 13% longer than the distance between their nodes; this increases to 40% for larger node separations.

• The distribution of filament widths is relatively narrow and shows a clear peak at $d = 3\text{h}^{-1}$Mpc. There are indications of an increase in the filament thickness as the filament length increases.

• Nodes are connected on average to 2 filaments, this number increases slightly with the node mass, reaching ≈ 3 filaments per node for masses close to $10^{15} M_\odot$

• In the infall region around nodes the average central skeleton density can be as high as a hundred times the mean density; at larger distances the density drops to a few times the mean density, and maintains a roughly constant value along $20 - 80\%$ of the filament length.

• There is a strong relation between length, quality, and straightness in the filament shape, where shorter filaments have better quality and are closer to straight-line geometries.

The filament properties we have studied in this work are focused on the general characteristics of filaments. There remain many specific properties of filaments and of their galaxy populations which can be related to several recent results such as (i) the halo clustering dependence on the halo mass and on its formation time (Gao, Springel & White 2005), (ii) the correlations between halo concentration and spin with the local environment (Avila-Reese et al. 2005), (iii) the fact that galaxy spins are strongly aligned along

filaments (Pimbblet 2005), (iv) the results using semi-analytic models obtained by González & Padilla (2009) which show several variations of galaxy properties with the local and large scale environment, as well as (v) other results showing that galaxy formation should be strongly dependent on large scale environment starting from their early stages of development, due for example to the delayed reionisation of filaments with respect to clusters as shown by hydro-simulations of the intracluster medium (Finlator et al. 2009). A first step will be to compare observational galaxy properties in filaments, in particular their colours, star-formation rates and luminosities with results from semi-analytic models, to characterise some of the previously mentioned environment effects.

Several studies of galaxy properties in clusters and voids have opened the possibility to expect important variations in the properties of haloes or galaxies while embedded in filament-like environments, since the populations of galaxies and haloes are very different in voids and clusters. By converging to a standard filament classification and detection method, the study of galaxy properties and halo assembly in filaments can be carried out with great detail to help understand the reasons behind these important population changes.

REFERENCES

Aragón-Calvo m., Jones B., van de Weygaert R., & van der Hulst J., 2007, A&A, 474, 315

Aragón-Calvo m., van de Weygaert R., Jones B. & van der Hulst J., 2007, ApJ, 655, L5

Avila-Reese V., Colin P., Gottlöber S., et al. 2005, ApJ, 634, 51

Barrow J., Sonoda H., & Bhavsar P. 1985. MNRAS, 216, 17

Bharadwaj S., Sahni V., Sathyaprakash B., et al. 2000, ApJ, 528, 21

Bharadwaj S., Bhavsar S. & Sheth J. 2004, ApJ, 606, 25

Biggs N., Lloyd E., Wilson R. 1986, "Graph Theory", 1736-1936, Oxford University Press.

Bond N., Strauss M. & Cen R. 2009, accepted for publication in ApJ

Bond R., Kofman L. & Pogosyan D. 1996, Nature, 380, 6575

Bullock J., Kolatt T., Sigad Y. et al. 2001, MNRAS, 321, 559

Colberg J., Krughoff K. & Connolly A., 2005, MNRAS, 359, 272

Colless M., Dalton G., Maddox S., et al. 2001, MNRAS, 328, 1039

Davis M., Efstathiou G., Frenk C., & White S. 1985, ApJ, 292, 371

Diaferio A. & Geller M. 1997, ApJ, 481, 633

Dietrich J., Schneider P., Clowe D., et al. 2005, A&A, 440, 2

Einasto J.,Klypin A., Saar E. & Shandarin S. 1984, MNRAS, 206, 529

Eriksen H., Novikov P., Lilje A., et al. 2004. AJ, 612, 64

Finlator K., Özel F., Davé R. 2009, accepted for publication in MNRAS

Gao L., Springel V. & White S. 2005, MNRAS, 363, 66

González R.E. & Padilla N.D. 2009, 397, 1498

Knollmann S., Knebe A. 2009, ApJS, 182, 608

Martínez V., & Saar E. 2002, Chapman & Hall/CRC, Boca Raton.

Mead J., King L. & McCarthy I. 2009, accepted for publication in MNRAS

Navarro J., Frenk C.S., White S.D.M 1997, ApJ, 490, 493.

Novikov D., Colombi S. & Doré O. 2006, MNRAS, 366, 1201

Padilla N., Ceccarelli L., Lambas D.G., 2005, MNRAS, 363, 977.

Pelupessy, F., Schaap, W., & van de Weygaert, R. 2003, A&A, 403, 309

Pimbblet, K., Drinkwater M., & Hawkrigg M. 2004, MNRAS, 354, L61

Pimbblet, K. 2005, MNRAS, 358, 256

Pivato M., Padilla N. & Lambas D. 2006, MNRAS, 373, 4

Porter S., Raychaudhury S., Pimbblet K., & Drinkwater M., 2008, MNRAS, 388, 1152

Sahni V., Sathyaprakash B., & Shandarin S. 1998, ApJ, 495, L5

Shaap W., & van de Weygaert R. 2000, A&A, 363, L29

Shandarin S. & Zel'dovich I. 1983, Comments on Astrophysics, 10, 33

Scharf C., Donahue M., Voit G. et al. 2000, ApJL, 528, L73

Sousbie T., Pichon C., Courtois H., et al. 2008, MNRAS, 383, 1655

Stoica R., Martinez V., Mateu J. & Saar E. 2005, A&A, 434, 423

Stoica R., Martinez V., Saar E. 2008, Appl. Statist., 56, 459

Stoughton C., Lupton R., Bernardi M., et al. 2002, AJ, 123, 485

Tittley E. & Henriksen M. 2001, Ap, 563, 673

Voronoi, G. 1908, Z. Reine Angew. Math, 134, 198

York D., et al. 2000, AJ, 120, 1579

Zel'dovich Y., 1970, A&A, 5, 84

Zel'dovich I., Einasto J. & Shandarin S. 1982, Nature, 300, 407

Zhang Y., Yang X., Faltenbacher A., et al. 2009, accepted for publication in ApJ